Nanoscale

ROYAL SOCIETY OF CHEMISTRY

PAPER

View Article Online
View Journal | View Issue

Cite this: *Nanoscale*, 2025, **17**, 16829

Verifying the efficient functional N species of metal-free N-doped carbons for CO_2-to-CO electrochemical conversion using zeolite-templated carbons with N species tuned by a recarbonization treatment†

Kotaro Narimatsu,[a] Ryuji Takada,*[a] Koji Miyake,*[a,b] Yoshiaki Uchida[a] and Norikazu Nishiyama[a,b]

The electrochemical reduction reaction of carbon dioxide is expected as a potential solution to reducing CO_2 emission and providing value-added chemicals. Carbon monoxide (CO) is a fundamental chemical precursor for industrially important reactions. Therefore, metal-free heteroatom-doped carbon materials have attracted increasing attention as electrocatalysts for CO_2-to-CO conversion. Nitrogen (N)-doped carbon is a promising alternative catalyst. The introduction of N atoms modifies the electronic and chemical structures and leads to enhanced electrocatalytic performance. While the bonding states of N species influence the CO_2RR activity has been discussed, no reports have demonstrated the relationship between the bonding state and activity by dividing graphitic N into two configurations (valley N and center N). In this study, we have controlled the local chemical state of N species of N-doped carbon materials through the combination of a zeolite templating method and a recarbonization treatment to investigate the effective functional N species for CO_2-to-CO conversion. When the recarbonization temperature increased, the content of valley N increased, and the CO_2-to-CO conversion was enhanced. The highest faradaic efficiency of CO was 76%. DFT calculations revealed that valley N and the edge site C atom adjacent to valley N stabilized *COOH intermediate, contributing to the enhanced CO_2-to-CO conversion.

Received 26th February 2025,
Accepted 3rd June 2025

DOI: 10.1039/d5nr00846h

rsc.li/nanoscale

Introduction

The electrochemical carbon dioxide reduction reaction (CO_2RR) operated using renewable energy has been regarded as an attractive solution to reducing the CO_2 accumulation in the atmosphere and providing value-added chemicals.[1–4] Among the CO_2RR products, carbon monoxide (CO) is a fundamental chemical precursor for industrially important reactions, such as methanol synthesis and Fischer Tropsch synthesis.[5–8] To date, great efforts have been made to develop metal-based electrocatalysts, such as Au,[9] Ag,[10] and Zn,[11] for CO_2 electroreduction into CO. However, the high cost or low durability of these metal-based catalysts prevent their widespread industrial implementation.[12,13] The development of alternative catalysts for CO_2-to-CO conversion is a highly desirable goal.

In recent years, nitrogen (N)-doped carbon materials for CO_2RR, such as single-atom catalysts[14,15] and metal-free catalysts (*e.g.*, nanodiamonds[16] and carbon quantum dots[17,18]) have attracted attention as promising alternative catalysts. In particular, metal-free nitrogen (N)-doped carbon materials for CO_2-to-CO conversion (*e.g.*, N-doped graphene[19,20] and carbon nanotubes[21,22]) have emerged as promising candidates for replacing metal-based catalysts. The introduction of N atoms modifies the electronic and chemical structure, leading to an enhancement of the electrocatalytic performance for the CO_2RR.[23,24] These materials have advantages: high stability, high conductivity, large specific surface areas and low cost.[25–27] The N species incorporated in the carbon matrix are divided into four main configurations, depending on their structural and electronic properties: graphitic N, pyridinic N, pyrrolic N and oxidized N.[28,29] Graphitic N is substituted for the C atom in the carbon matrix by bonding it to three C atoms, which should be differentiated into two configurations.

[a]*Division of Chemical Engineering, Graduate School of Engineering Science, Osaka University, 1-3 Machikaneyama, Toyonaka, Osaka 560-8531, Japan. E-mail: kojimiyake@cheng.es.osaka-u.ac.jp*
[b]*Innovative Catalysis Science Division, Institute for Open and Transdisciplinary Research Initiatives (ICS-OTRI), Osaka University, Suita 565-0871, Japan*
† Electronic supplementary information (ESI) available. See DOI: https://doi.org/10.1039/d5nr00846h

One located in the edge site is called valley N and the other located on the graphene basal plane is called center N.[30,31] However, no reports have suggested how the two configurations of graphitic N affect the catalytic activity for CO_2RR. In addition, it is difficult to control the doping content because of the necessity of high-temperature heat treatment during the synthesis of carbon materials. Therefore, we focused on the zeolite templating method as an effective synthesis method to form abundant pores and defects for the control of the N-doping content.[32] In prior research, we applied a zeolite templating method using pyridine (C and N precursors) for the synthesis of pyridinic N-rich carbon materials.[33,34] Furthermore, to increase the valley N content, we also focused on recarbonization treatment. Generally, it is known that pyridinic N changes into valley N or center N, resulting in more stable N configurations owing to high-temperature heat treatment. Therefore, it should be possible to synthesize N-doped carbon materials with different content of pyridinic N, valley N and graphitic N by using both a zeolite templating method and a recarbonization treatment at the optimum temperature.

In this study, we controlled the local chemical state of N species in N-doped carbon materials through a combination of a zeolite templating method with pyridine and a recarbonization treatment. This is the first study to demonstrate that metal-free N-doped carbon materials prepared by zeolite templating can electrochemically catalyze CO_2 into CO by controlling the proportion of N species. In addition, experimental analysis and density functional theory (DFT) calculation provided new insights into the effect of valley N on CO_2RR activity.

Experimental

Materials

NaOH (4 M), HCl (5 M), pyridine and Nafion (5 wt%) were obtained from Wako Pure Chemical Industries. Protonated FAU-type zeolite (HY) with a Si/Al = 3.6 was obtained from Tosoh.

Preparation of N-doped carbons (NDCs)

The overall synthetic strategy is based on our previous studies.[33,34] HY (0.3 g) was annealed under N_2 flow at 800 °C for 1 h. The chemical vapor deposition treatment of a pyridine vapor at the saturated vapor pressure at 0 °C was performed for 5 h. The obtained zeolite-carbon composite was named "HY/NDC". HY/NDC was treated at 180 °C in NaOH (4 M) aqueous solution overnight. Then, the suspension was filtered and the collected solid was washed by deionized water. Then, the resultant powder was rinsed in HCl (5 M) aqueous solution. Moreover, until the solution became neutral, the solid powder was repeatedly rinsed by deionized water. Finally, the solid powder was dried at 90 °C overnight and was carbonized under N_2 flow at T °C (T = 900, 1000, and 1100) for 3 h. The carbonization treatment is called recarbonization in this study. After the recarbonization, the samples are denoted as "NDC-T".

Characterizations

Scanning electron microscope-energy dispersive X-ray spectrometry (SEM-EDX) was performed using a JCM-7000 (JEOL, Japan) and Transmission electron microscope (TEM) was carried out using an H800 (Hitachi, Japan). X-ray diffraction (XRD) was conducted on a PANalytical X'Pert-MDR diffractometer using Cu Kα radiation. N_2 adsorption isotherms at 77 K were recorded using a BELSORP MINI X (Microtrac MRB, Japan). Consequently, pore volumes, pore size distributions, and the specific surface areas were determined based on the BJH (Barrett–Joyner–Halenda), MP-Plot and Brunauer Emmett Teller (BET) methods. Analysis for C, H and N contents was conducted using FlashEA (Thermo Fisher Scientific, USA). X-ray photoelectron spectroscopic (XPS) was conducted using a Kratos Ultra 2 (Shimadzu, Japan).

Electrochemical measurements

Isopropanol, Nafion (5 wt% in alcohol and water) and water were mixed in a volume ratio of 1 : 1 : 8. A catalyst (5 mg) was suspended in the solution (500 μL), and the suspension was ultrasonicated to obtain the catalyst ink. The ink (100 μL) was pipetted on a carbon paper. The mass loading of a catalyst on the carbon paper was fixed at 1 mg cm^{-2}. A Biologic SP-50e potentiostat (TOYO, Japan) was used as an electrochemical analyzer. An as-prepared working electrode, Ag/AgCl (reference electrode), and a platinum wire (counter electrode) were equipped at a H-type cell. The potentials in this study are relative to the reversible hydrogen electrode (RHE), based on the equations below:

$$E_{RHE} = E_{Ag/Agcl} + 0.208 + 0.0591 \times pH$$

Linear sweep voltametric (LSV) measurements with a scan rate of 5 mV s^{-1} were performed in CO_2-saturated and N_2-saturated 0.1 M $KHCO_3$ solution, and the potential range was from 0.15 V to −1.2 V *vs.* RHE. During the LSV measurements, CO_2 and N_2 keep flowing. CO_2 splitting experiments were carried out in a CO_2-saturated 0.1 M $KHCO_3$ solution with stirring at 350 rpm. Before CO_2 splitting experiments, the 0.1 M $KHCO_3$ solution was pre-saturated with CO_2 for at least 30 minutes. The gas-phase products were quantified by offline gas chromatography (GC) (GC-8A, Shimadzu, Japan) using a Shincarbon-ST column (SHINWA, Japan). The products in a liquid phase were detected using an ^{1}H NMR (ECS, JEOL, Japan). The below equations were applied to calculate the faradaic efficiencies of the gas products:

$$FE = \frac{\text{moles of products}}{Q/nF} \times 100\%$$

FE (%) = faradaic efficiency; Q (C) = electric quantity; n (–) = electron transfer number; F (C mol^{-1}) = Faraday constant, 96 485.33 C mol^{-1}

Density functional theory (DFT) calculations

B3YLYP hybrid DFT of Gaussian 16W[35] was conducted with a basis set of 6-31G (d, p) to obtain the stabilized model, the atomic population, and the various thermodynamic energy. Several possible heteroatoms doped carbon configurations, containing pyridinic N, center N, and valley N, were used as calculated models in this study. The ground state structures of *COOH and *CO adsorbed on heteroatoms doped carbon model were identified by finding the lowest energy one among several possible configurations on N atoms and C atoms adjacent to N atoms as possible active sites.

The below equation was applied for calculating adsorption energy:

$$E_{ads} = E_{complex} - E_{substrate} - E_{adsorbate}$$

where E_{ads}, $E_{complex}$, $E_{substrate}$, and $E_{adsorbate}$ are the adsorption energy of adsorbate (*COOH, *CO) on substrate (heteroatoms doped carbon), the total energy of adsorbate on substrate, the total energy of substrate, and the total energy of adsorbate.

According to computational hydrogen electrode (CHE) model, the Gibbs free energy was calculated by the following equation:

$$\Delta G = \Delta E_{ads} + \Delta E_{ZPE} - T\Delta S$$

where ΔE_{ads} is different adsorption energy of adsorbate, ΔE_{ZPE} is zero-point energy changes calculated by the vibration frequency of each adsorbate, T is temperature (298.15 K), and ΔS is entropy change of the reaction.

In this work, the reaction pathway of CO_2 electroreduction into CO was based on following elementary step:

$$* + CO_2\ (g) + H^+ + e^- \rightarrow *COOH$$

$$*COOH + H^+ + e^- \rightarrow *CO + H_2O\ (l)$$

$$*CO \rightarrow * + CO\ (g)$$

As the first intermediate of CO_2RR, not only *COOH but also *CO_2- and *OCHO are considered, however, as regards CO production, *COOH is considered as the main first intermediate of CO_2-to-CO conversion.[3,36,37] So, *COOH was chosen as the first intermediate of CO_2RR in this work.

Results & discussion

NDCs were prepared by the zeolite templating method using Y zeolite as a template and pyridine as C and N precursors. Y zeolite was heated under N_2 atmosphere at 800 °C, and the CVD treatment of the pyridine vapor was conducted for 5 h. The obtained zeolite-carbon composite was denoted as HY/NDC. First, XRD measurement was performed to investigate the crystal structures of HY/NDC. HY/NDC exhibited a peak similar to those of a pristine protonated FAU-type zeolite (HY) as shown in Fig. S1,† suggesting that the crystal structure of zeolite template was not decomposed during the CVD process. The EDX analysis indicated that there is hardly any detection

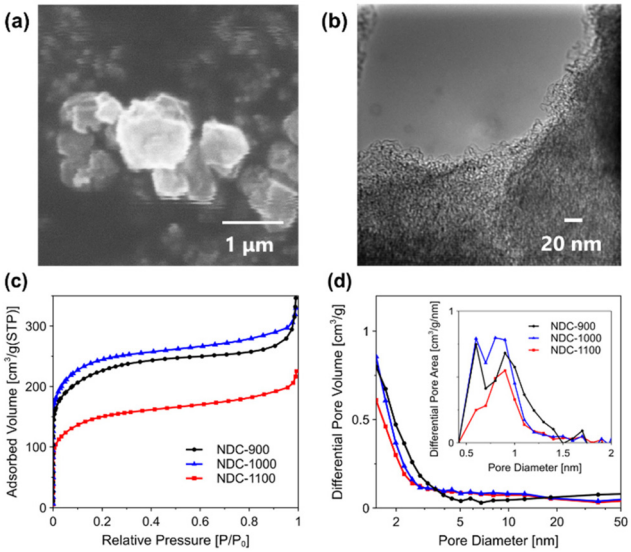

Fig. 1 (a) SEM and (b) TEM images of NDC-1100. (c) N_2 adsorption isotherms and (d) pore size distributions of NDC-*T*.

of Si and Al in NDC-*T*, suggesting that base and acid treatments removed zeolite contained in HY/NDC (Table S1†). In addition, the morphologies and pores of synthesized NDC-*T* were investigated by TEM and SEM-EDX. As shown in Fig. 1a and Fig. S2,† the morphology of each sample was similar to that of the zeolite template. Moreover, the pore structures of NDC-*T* were observed by TEM (Fig. 1b and Fig. S3†), it was revealed that the structure of NDC-1100 was sparser than that of HY/NDC, as shown in Fig. S3.†

As shown in Fig. 1c, the result of N_2 adsorption isotherms indicated that the adsorption volume in the low relative pressure region (lower than 0.01), which is assigned to the adsorption of micropores, declined on NDC-1100 compared to NDC-1000. The high-temperature recarbonization treatment may cause a decline in the microporosity. The graphene microscale defects on a graphene lattice are aligned during high-temperature recarbonization treatment, leading to shrinking of the micropores. Moreover, Fig. 1d shows the pore size distributions based on MP-plot and BJH methods. Micropores (~2 nm) were identified in NDC-*T*. The most abundant micropore family was centered at 0.9 nm. It is known that the space originally occupied by the zeolite framework provides a microporous structure with a uniform micropore size (theoretically approximately 1.2 nm).[38] The mode pore diameters were close to the theoretical pore sizes. These results confirmed that pores derived from the zeolite template were formed in NDC-*T*. Moreover, Table S2† shows the BET areas, and each pore volume based on MP-plot and BJH methods. There was no correlation between the pore volume and recarbonization temperature. Fig. S4† shows the XRD patterns of NDC-*T*. All samples exhibited two broad peaks at 23.8° and 43.4° assigned to the (002) and (100) planes of carbon, which originated from the crystalline nature of carbon.[39,40]

Table 1 CHN elemental analysis results of NDC-T

Sample	C [wt%]	H [wt%]	N [wt%]
NDC-900	67.10	1.97	2.75
NDC-1000	72.63	1.18	2.64
NDC-1100	76.84	1.55	2.77

The amount of nitrogen in NDC-*T* determined by The CHN elemental analysis (Table 1) was approximately 2–3 wt%. The results showed that sufficient nitrogen was present in the carbon materials after recarbonization at *T* °C. However, similar nitrogen contents were obtained for any of the samples.

The bonding states of the NDC-*T* surfaces were investigated using XPS measurements. As displayed in Fig. 2a, it was carried out regarding the XPS on N 1s spectra that a deconvolution into five peaks in the half-width at half-maximum range from 0.8 eV to 1.2 eV, so that each peak position is aligned for our samples (pyridinic N: ~398.1 eV, pyrrolic N: 399.7 eV, center N: 401.0 eV, valley N: 402.2 eV, oxidized N: 404.0~ eV).[41,42] In addition, as shown in Fig. S5,† it was identified that each proportion of pyrrolic N and pyridinic N declined by carbonization. These results revealed that recarbonization caused a change in the carbon structure, and the proportion of N species was changed by recarbonization at various temperatures. Generally, pyrrolic N is known to be more unstable than other N species, such as pyridinic N and graphite N (center N and valley N) at relatively high temperature (>873 K), is converted to pyridinic N and graphitic N.[31] Furthermore, Fig. 2b shows the proportion of N species in NDC-*T*. The results indicate that the bonding states of NDC-*T* differed with respect to the recarbonization temperature. With increasing recarbonization temperature, the proportion of center N, valley N, and oxidized N increased, while those of pyridinic N and pyrrolic N decreased.

The electrocatalytic performance on the CO_2RR was evaluated by electrochemical measurements in an H-type cell. LSV measurements were conducted in both N_2-saturated and CO_2-saturated 0.1 M $KHCO_3$ solution using NDC-1100. NDC-1100 showed a higher current density in CO_2-saturated 0.1 M $KHCO_3$ solution than that in N_2-saturated 0.1 M $KHCO_3$ solution at a positive potential than −0.9 V *vs.* RHE (Fig. 3a), suggesting high catalytic activity for CO_2RR. On the other hand, a higher current density was obtained in N_2-saturated 0.1 M $KHCO_3$ solution than that in CO_2-saturated 0.1 M $KHCO_3$ solution at a negative potential than −0.9 V *vs.* RHE, suggesting the hydrogen evolution reaction (HER) is dominant. Moreover, comparing the current density of NDC-*T* in CO_2-saturated 0.1 M $KHCO_3$ solution, it was found that the current density in CO_2-saturated 0.1 M $KHCO_3$ solution increased by increasing recarbonization temperature (Fig. 3b). It is expected that the differences in the proportion of N species in NDC-*T* cause changes in the charge density distribution, providing high electrical conductivity and catalytically active sites.

Furthermore, the selectivity of electroreduction products for NDC-*T* at various potentials was investigated using a controlled potential electrolysis method. The measurement was conducted at potentials in 0.1 V increments from −0.5 to −0.8 V *vs.* RHE for 1.5 h. The products in liquid phase obtained for the experiment were investigated by ^{1}H NMR, but it was below the detection limit. The electroreduction products were confirmed to be only gas-phase products. Products in the gas phase, mainly CO and H_2, were yielded within the potential window from −0.5 V to −0.8 V *vs.* RHE. The FE_{CO} of NDC-*T* was the highest at −0.7 V *vs.* RHE (Fig. 3c), suggesting that NDC-*T* promoted the CO_2RR and suppressed the HER. Whereas the FE_{CO} decreased gradually as the applied potential changed (less or more than −0.7 V *vs.* RHE), which means the dominance of the HER over the CO_2RR. Moreover, comparing the FE_{CO} at −0.7 V *vs.* RHE, it was identified that the faradaic efficiency of CO (FE_{CO}) for NDC-*T* increased by carbonization (Fig. S6†). In addition, the FE_{CO} for NDC-*T* increased with increasing recarbonization temperature, suggesting that center N and valley N could contribute to the improvement of CO_2RR performance. NDC-1100 exhibited the highest FE_{CO} of 76%, which is consistent with the results of the LSV measurements (Fig. 3a). Compared to our best catalyst (NDC-1100, the FE_{CO} of 76%), other metal-free N-doped carbon materials reported recently, such as GM2,[43] PPc/CNT,[36] and ZNMC-30,[44] exhibited the highest FE_{CO} of 87.6%, 98.8%, and 88.9%. Therefore, our catalysts still have the potential to improve CO_2-to-CO conversion performance. However, this catalyst synthesis method represents a breakthrough in that it enables the precise control of the local chemical state of N species in N-doped carbon while maintaining a nearly constant nitrogen content. To confirm the carbon source of products by CO_2RR, the electrolysis experiment was conducted on NDC-1100 in N_2-saturated 0.1 M $KHCO_3$ solution at −0.7 V *vs.* RHE. Only H_2 is detected in the gas-phase product (Fig. S7†), suggesting that the CO_2 dissolved in the electrolyte was the only carbon source for producing CO. Furthermore, to investigate the influence of carbon paper, the electrolysis experiment was conducted in CO_2-saturated 0.1 M $KHCO_3$ solution at −0.7 V *vs.* RHE. In the gas-phase product, only H_2 was detected (Fig. S8†). The results confirmed that carbon paper itself did not produce CO in the CO_2RR electrolysis experiment.

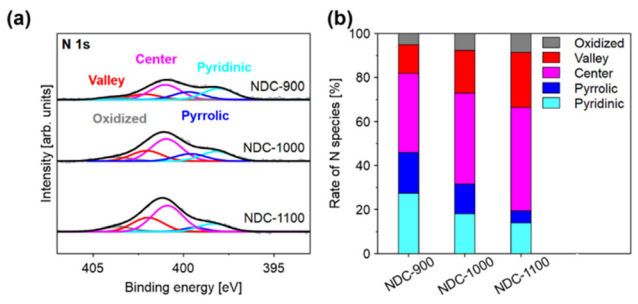

Fig. 2 (a) XPS spectra (N 1s) of NDC-*T* and (b) the rate of N species in NDC-*T*.

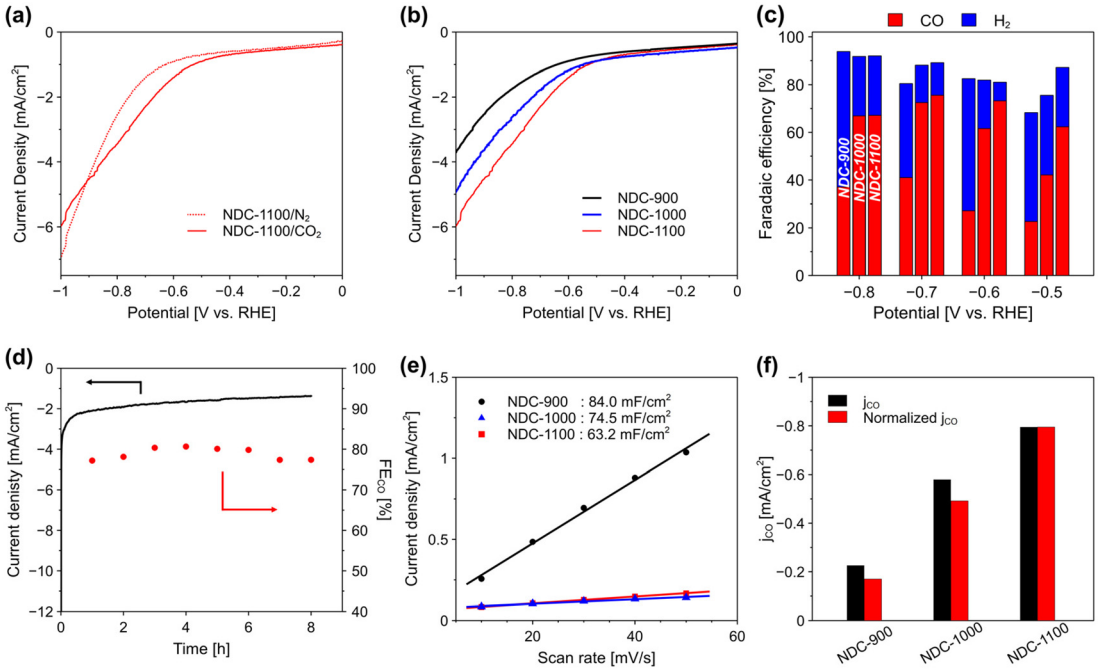

Fig. 3 (a) LSV curves in N_2-saturated and CO_2-saturated 0.1 M $KHCO_3$ solution using NDC-1100 as an electrocatalyst. (b) LSV curves in CO_2-saturated 0.1 M $KHCO_3$ solution using each catalyst. (c) faradaic efficiencies of CO and H_2 using NDC-*T* within the potential window from −0.5 V to −0.8 V *vs.* RHE in CO_2-saturated 0.1 M $KHCO_3$ solution. (d) Chronoamperometric responses and faradaic efficiency of CO and H_2 on NDC-1100 at −0.7 V *vs.* RHE for 8 h in CO_2-saturated 0.1 M $KHCO_3$ solution. (e) Double-layer capacitance values of each catalyst. (f) The comparison of partial current density of CO (j_{CO}; black bar) and the j_{CO} normalized by ECSA (normalized j_{CO}; red bar) of each catalyst at −0.7 V *vs.* RHE.

Besides the selectivity of electroreduction products, the durability of the CO_2RR catalysts is a crucial parameter for practical applications. The chronoamperometric response was performed on NDC-1100 at −0.7 V *vs.* RHE for 8 h (Fig. 3d). The current density slightly declined under continuous operation for up to 8 h because of catalyst stripping from the carbon paper and coating of the catalyst surface with gaseous products. Meanwhile, no decay of FE_{CO} was identified after continuous test for 8 h, suggesting that the NDC-1100 is a stable electrocatalyst for CO_2RR.

Various comparisons were conducted to clarify the effects by the difference of the N species proportion based on experimental results. As shown in Table S2,† although NDC-1100 had a lower BET surface area than that of NDC-900 and NDC-1000, the FE_{CO} of NDC-1100 was higher than that of NDC-900 and NDC-1000 (Fig. 3c). In addition, Table 1 shows no significant differences in the nitrogen content of the NDC-*T*. Therefore, it is expected that the difference in the proportion of N species has a more significant effect on activity than the other properties. To verify this, the double-layer capacitance derived from cyclic voltammetry at different scan rates was measured for estimating the electrochemical surface area (ECSA) as shown in Fig. S9.† As shown in Fig. 3e, NDC-1100 exhibited the smallest ECSA of all catalysts. Furthermore, the current density generated by the production of CO (j_{CO}) at −0.7 V *vs.* RHE normalized by ECSA was calculated (Fig. 3f). The normalized j_{CO} of NDC-*T* increased with the recarbonization temperature. We also investigated the relationship between j_{CO} and the content of each N species. As shown in Fig. S10a,† j_{CO} decreased with increasing pyridinic N. Meanwhile, there is a positive correlation between j_{CO} and the content of center N and valley N (Fig. S10b and c†). In particular, the best relationship was obtained between j_{CO} and the content of valley N. For these reasons, it is considered that valley N should favorably contribute to the improvement of CO_2RR activity.

DFT calculations using Gaussian were performed to gain further insight into the CO_2RR mechanisms on N-doped carbon. Introducing N atom into carbon matrix could modify the electronic and chemical structure.[23,24] It is suggested that center N and valley N had a good influence on the CO_2RR activity based on experimental analysis (Fig. 2b, 3c and Fig. S10†). In addition, pyridinic N is regarded as an active site for several electrochemical reactions.[20,21,45] For these reasons, three N-doped carbon configurations, containing pyridinic N, center N, and valley N each, were used as calculated models (Fig. 4a). The reaction pathways for the electroreduction of CO_2 to CO are shown in Fig. S11.† The ground state structures of *COOH and *CO adsorbed on N-doped carbon models were identified by finding the lowest free energy one among several possible configurations on N atoms and C atoms adjacent to N atoms as possible active sites.

The corresponding Gibbs free energy diagrams and reaction pathways for CO_2RR to CO are shown in Fig. 4b and Fig. S11.†

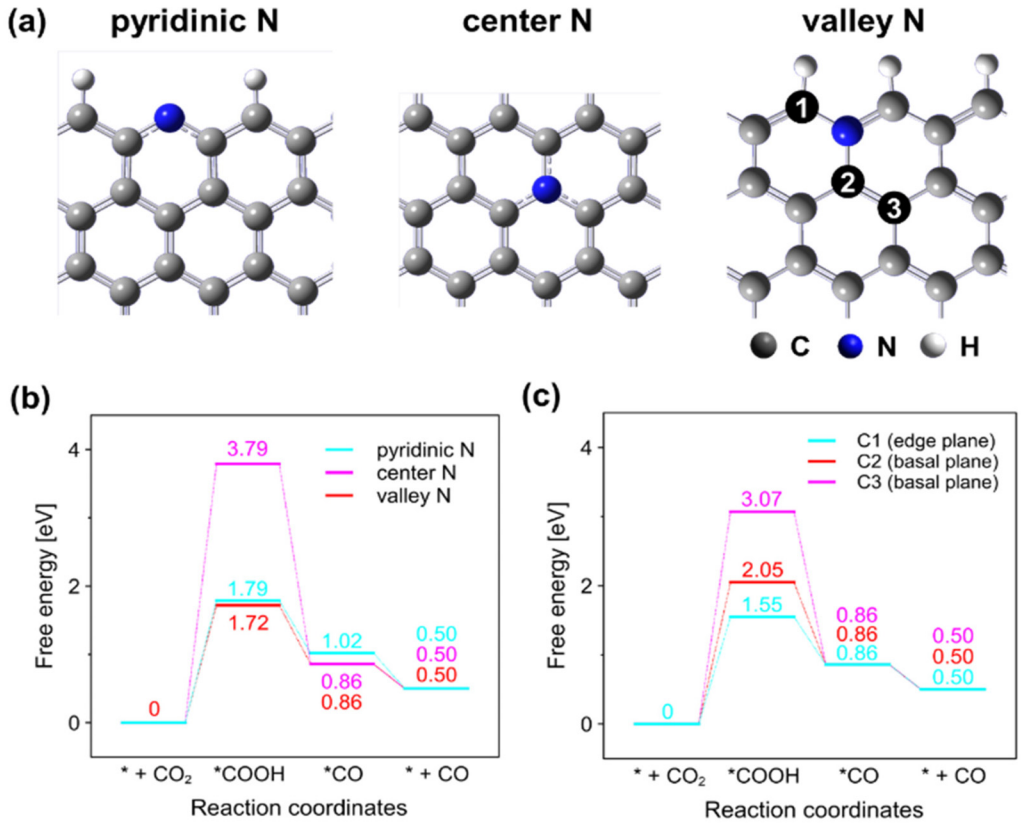

Fig. 4 (a) The computational structure models of three N-doped carbon configurations, containing pyridinic N, center N, and valley N each. (b) Gibbs free energy diagrams for CO_2RR to CO on N atom on three N-doped carbon configurations. (c) Gibbs free energy diagrams for CO_2RR to CO on three C atom configurations adjacent to valley N.

First, N atoms on N-doped carbon models were employed as the active sites. The free energy diagrams were constructed at 0 V *vs.* RHE according to the computational hydrogen electrode model.[46] As shown in Fig. 4b, it was revealed that the rate-determining step on N-doped carbon models was *COOH adsorption of the first step. Moreover, the free energy barriers of 1.72 eV on model valley N and 1.79 eV on model pyridinic N were much lower than that of 3.79 eV on model center N, suggesting that the edge site N species contributed to stabilizing *COOH intermediate. Therefore, in addition to pyridinic N, valley N is also regarded as a candidate active site on N-doped carbon. Considering based on experimental results in addition to DFT calculations results, valley N is considered to be a more favorable active site rather than pyridinic N because the FE_{CO} for NDC-*T* increased as the increase of valley N and the decrease of pyridinic N (Fig. 2b and 3c).

Furthermore, to gain further insight into the effect of valley N on CO_2RR, C atoms adjacent to valley N were employed as active sites. As shown in Fig. 4a, three C atom configurations, C1 located on edge planes and C2 and C3 located on the basal planes, were used as the calculated models. The corresponding Gibbs free energy diagrams and reaction pathways for CO_2RR to CO are displayed in Fig. 4c and Fig. S12.† The free energy barriers of 1.55 eV on C1 located on edge planes were lower than that of 2.05 eV on C2 and 3.07 eV on C3 located on basal planes, suggesting that the edge site C atom adjacent to valley N stabilized *COOH intermediate. In contrast, the *CO adsorption energy of the second step was the same (0.86 eV) for all C configurations. Based on these DFT calculation results, a new insight into the effect of N species on CO_2RR activity was provided that valley N and edge site C atoms adjacent to valley N can be more favorable active sites than other N atoms on N species.

Conclusions

N-doped carbons (NDC-*T*) were synthesized with various edge site N contents by combining a zeolite templating method and a recarbonization treatment. We succeeded in controlling the local chemical state of N species of N-doped carbons by changing recarbonization temperatures. The obtained NDC-*T* electrochemically catalyzed CO_2 to CO, and the best catalyst, NDC-1100, exhibited the highest FE_{CO} of 76%. Furthermore, experimental analysis and DFT calculations revealed that valley N and the edge site C atom adjacent to valley N stabilized *COOH intermediate, contributed to improvement of CO_2RR activity. Our work provides not only a rational design

method for N-doped carbons to control the proportion of N species but also new insights into the effect of valley N on CO_2RR activity.

Author contributions

Kotaro Narimatsu: investigation, visualization, writing – original draft. Ryuji Takada: conceptualization, investigation, visualization, methodology, writing – review & editing. Koji Miyake: conceptualization, supervision, visualization, methodology, writing – review & editing. Yoshiaki Uchida: writing – review & editing. Norikazu Nishiyama: supervision, resources, writing – review & editing.

Data availability

The data supporting this article have been included as part of the ESI.†

Conflicts of interest

There are no conflicts to declare.

Acknowledgements

The study was partially conducted using a facility at the Research Center for Ultra-High Voltage Electron Microscopy, Osaka University, Suita, Japan.

References

1 Q. Lin, X. Zhang, T. Wang, C. Zheng and X. Gao, *Engineering*, 2022, **14**, 27–32.
2 X. Tan, C. Yu, Y. Ren, S. Cui, W. Li and J. Qiu, *Energy Environ. Sci.*, 2021, **14**, 765–780.
3 Y. Y. Birdja, E. Pérez-Gallent, M. C. Figueiredo, A. J. Göttle, F. Calle-Vallejo and M. T. M. Koper, *Nat. Energy*, 2019, **4**, 732–745.
4 M.-Y. Lee, K. T. Park, W. Lee, H. Lim, Y. Kwon and S. Kang, *Crit. Rev. Environ. Sci. Technol.*, 2020, **50**, 769–815.
5 S. Lu, Y. Shi, N. Meng, S. Lu, Y. Yu and B. Zhang, *Cell Rep. Phys. Sci.*, 2020, **1**, 100237.
6 L. Delafontaine, T. Asset and P. Atanassov, *ChemSusChem*, 2020, **13**, 1688–1698.
7 K. Gan, H. Li, R. Li, J. Niu, J. He, D. Jia and X. He, *Inorg. Chem. Front.*, 2023, **10**, 2414–2422.
8 L. Luo, Z. Huang and Q. Tang, *J. Mater. Chem. A*, 2024, **12**, 5145–5155.
9 J. Fu, Y. Wang, J. Liu, K. Huang, Y. Chen, Y. Li and J.-J. Zhu, *ACS Energy Lett.*, 2018, **3**, 946–951.
10 J. Gao, S. Zhao, S. Guo, H. Wang, Y. Sun, B. Yao, Y. Liu, H. Huang and Z. Kang, *Inorg. Chem. Front.*, 2019, **6**, 1453–1460.
11 X. Y. Zhang, W. J. Li, J. Chen, X. F. Wu, Y. W. Liu, F. Mao, H. Y. Yuan, M. Zhu, S. Dai, H. F. Wang, P. Hu, C. Sun, P. F. Liu and H. G. Yang, *Angew. Chem., Int. Ed.*, 2022, **61**, e202202298.
12 I. Masood ul Hasan, L. Peng, J. Mao, R. He, Y. Wang, J. Fu, N. Xu and J. Qiao, *Carbon Energy*, 2021, **3**, 24–49.
13 X. Duan, J. Xu, Z. Wei, J. Ma, S. Guo, S. Wang, H. Liu and S. Dou, *Adv. Mater.*, 2017, **29**, 1701784.
14 Y. Zhang, J. Zhao and S. Lin, *Chin. J. Struct. Chem.*, 2024, **43**, 100415.
15 M. Humayun, M. Bououdina, A. Khan, S. Ali and C. Wang, *Chin. J. Struct. Chem.*, 2024, **43**, 100193.
16 Y. Liu, S. Chen, X. Quan and H. Yu, *J. Am. Chem. Soc.*, 2015, **137**, 11631–11636.
17 T. Zhang, W. Li, K. Huang, H. Guo, Z. Li, Y. Fang, R. M. Yadav, V. Shanov, P. M. Ajayan, L. Wang, C. Lian and J. Wu, *Nat. Commun.*, 2021, **12**, 5265.
18 R. M. Yadav, Z. Li, T. Zhang, O. Sahin, S. Roy, G. Gao, H. Guo, R. Vajtai, L. Wang, P. M. Ajayan and J. Wu, *Adv. Mater.*, 2022, **34**, 2105690.
19 H. Wang, Y. Chen, X. Hou, C. Ma and T. Tan, *Green Chem.*, 2016, **18**, 3250–3256.
20 J. Wu, M. Liu, P. P. Sharma, R. M. Yadav, L. Ma, Y. Yang, X. Zou, X.-D. Zhou, R. Vajtai, B. I. Yakobson, J. Lou and P. M. Ajayan, *Nano Lett.*, 2016, **16**, 466–470.
21 J. Wu, R. M. Yadav, M. Liu, P. P. Sharma, C. S. Tiwary, L. Ma, X. Zou, X.-D. Zhou, B. I. Yakobson, J. Lou and P. M. Ajayan, *ACS Nano*, 2015, **9**, 5364–5371.
22 K.-H. Liu, H.-X. Zhong, X.-Y. Yang, D. Bao, F.-L. Meng, J.-M. Yan and X.-B. Zhang, *Green Chem.*, 2017, **19**, 4284–4288.
23 C. Chen, X. Sun, X. Yan, Y. Wu, H. Liu, Q. Zhu, B. B. A. Bediako and B. Han, *Angew. Chem.*, 2020, **132**, 11216–11222.
24 B. Zhang, J. Zhang, F. Zhang, L. Zheng, G. Mo, B. Han and G. Yang, *Adv. Funct. Mater.*, 2020, **30**, 1906194.
25 G. An, K. Wang, Z. Wang, M. Zhang, H. Guo and L. Wang, *ACS Appl. Mater. Interfaces*, 2024, **16**, 29060–29068.
26 Y. Dong, Q. Zhang, Z. Tian, B. Li, W. Yan, S. Wang, K. Jiang, J. Su, C. W. Oloman, E. L. Gyenge, R. Ge, Z. Lu, X. Ji and L. Chen, *Adv. Mater.*, 2020, **32**, 2001300.
27 Q. Zhai, H. Huang, T. Lawson, Z. Xia, P. Giusto, M. Antonietti, M. Jaroniec, M. Chhowalla, J.-B. Baek, Y. Liu, S. Qiao and L. Dai, *Adv. Mater.*, 2024, **36**, 2405664.
28 M. Inagaki, M. Toyoda, Y. Soneda and T. Morishita, *Carbon*, 2018, **132**, 104–140.
29 D. Guo, R. Shibuya, C. Akiba, S. Saji, T. Kondo and J. Nakamura, *Science*, 2016, **351**, 361–365.
30 H. Kiuchi, R. Shibuya, T. Kondo, J. Nakamura, H. Niwa, J. Miyawaki, M. Kawai, M. Oshima and Y. Harada, *Nanoscale Res. Lett.*, 2016, **11**, 127.
31 T. Sharifi, G. Hu, X. Jia and T. Wågberg, *ACS Nano*, 2012, **6**, 8904–8912.

32 H. Nishihara and T. Kyotani, in *Novel Carbon Adsorbents*, ed. J. M. D. Tascón, Elsevier, Oxford, 2012, pp. 295–322.
33 Y. Taniguchi, S. Kokuryo, R. Takada, X. Yang, K. Miyake, Y. Uchida and N. Nishiyama, *Electrochem. Commun.*, 2024, **160**, 107665.
34 Y. Taniguchi, S. Kokuryo, R. Takada, X. Yang, K. Miyake, Y. Uchida and N. Nishiyama, *Carbon Rep.*, 2024, **3**, 11–17.
35 M. J. Frisch, G. W. Trucks, H. B. Schlegel, G. E. Scuseria, M. A. Robb, J. R. Cheeseman, G. Scalmani, V. Barone, G. A. Petersson, H. Nakatsuji, X. Li, M. Caricato, A. V. Marenich, J. Bloino, B. G. Janesko, R. Gomperts, B. Mennucci, H. P. Hratchian, J. V. Ortiz, A. F. Izmaylov, J. L. Sonnenberg, F. Williams, F. Ding, F. Lipparini, J. Egidi, B. Goings, A. Peng, T. Petrone, D. Henderson, V. G. Ranasinghe, J. Zakrzewski, N. Gao, G. Z. Rega, W. Liang, M. Hada, M. Ehara, K. Toyota, R. Fukuda, J. Hasegawa, M. Ishida, T. Nakajima, Y. Honda, O. Kitao, H. Nakai, T. Vreven, K. Throssell, J. A. Montgomery Jr, J. E. Peralta, F. Ogliaro, M. J. Bearpark, J. J. Heyd, E. N. Brothers, K. N. Kudin, V. N. Staroverov, T. A. Keith, R. Kobayashi, J. Normand, K. Raghavachari, A. P. Rendell, J. C. Burant, S. S. Iyengar, J. Tomasi, M. Cossi, J. M. Millam, M. Klene, C. Adamo, R. Cammi, J. W. Ochterski, R. L. Martin, K. Morokuma, O. Farkas, J. B. Foresman and D. J. Fox, *Gaussian16 Rev. C. 01*, Wallingford, CT, 2016; C. Lee, W. Yang and R. G. Parr, *Phys. Rev. B*, 1988, **37**, 785–789**https://gaussian.com/news/** (accessed February 7, 2025).
36 W. Li, C. Yu, X. Song, X. Tan, H. Xu, Y. Ren, S. Cui, Y. Zhang, J. Chang, Y. Ding, Y. Xie and J. Qiu, *Chem. Mater.*, 2024, **36**, 1602–1611.
37 W. Zheng, D. Wang, Y. Zhang, S. Zheng, B. Yang, Z. Li, R. D. Rodriguez, T. Zhang, L. Lei, S. Yao and Y. Hou, *Nano Energy*, 2023, **105**, 107980.
38 H. Nishihara and T. Kyotani, *Chem. Commun.*, 2018, **54**, 5648–5673.
39 L.-L. Ling, L. Jiao, X. Liu, Y. Dong, W. Yang, H. Zhang, B. Ye, J. Chen and H.-L. Jiang, *Adv. Mater.*, 2022, **34**, 2205933.
40 W. Wang, L. Shang, G. Chang, C. Yan, R. Shi, Y. Zhao, G. I. N. Waterhouse, D. Yang and T. Zhang, *Adv. Mater.*, 2019, **31**, 1808276.
41 Q. Lai, J. Zheng, Z. Tang, D. Bi, J. Zhao and Y. Liang, *Angew. Chem.*, 2020, **132**, 12097–12104.
42 J. Quílez-Bermejo, E. Morallón and D. Cazorla-Amorós, *Chem. Commun.*, 2018, **54**, 4441–4444.
43 S. Liu, H. Yang, X. Huang, L. Liu, W. Cai, J. Gao, X. Li, T. Zhang, Y. Huang and B. Liu, *Adv. Funct. Mater.*, 2018, **28**, 1800499.
44 J. Zhang, K. Wang, X. Wang and X. Li, *ACS Appl. Mater. Interfaces*, 2024, **16**, 54092–54104.
45 P. P. Sharma, J. Wu, R. M. Yadav, M. Liu, C. J. Wright, C. S. Tiwary, B. I. Yakobson, J. Lou, P. M. Ajayan and X.-D. Zhou, *Angew. Chem., Int. Ed.*, 2015, **54**, 13701–13705.
46 A. A. Peterson, F. Abild-Pedersen, F. Studt, J. Rossmeisl and J. K. Nørskov, *Energy Environ. Sci.*, 2010, **3**, 1311.